

See discussions, stats, and author profiles for this publication at: <https://www.researchgate.net/publication/43097428>

# Metallophosphazene Precursor Routes to the Solid-State Deposition of Metallic and Dielectric Microstructures and Nanostructures on Si and SiO<sub>2</sub>

ARTICLE *in* LANGMUIR · APRIL 2010

Impact Factor: 4.46 · DOI: 10.1021/la100371w · Source: PubMed

---

CITATIONS

12

READS

31

## 7 AUTHORS, INCLUDING:



[Carlos Diaz](#)

University of Santiago, Chile

48 PUBLICATIONS 420 CITATIONS

[SEE PROFILE](#)



[María Luisa Valenzuela Valdés](#)

Universidad Autónoma De Chile

52 PUBLICATIONS 376 CITATIONS

[SEE PROFILE](#)



[Vladimir Lavayen](#)

Universidade Federal do Rio Grande do Sul

46 PUBLICATIONS 586 CITATIONS

[SEE PROFILE](#)



[Colm O'Dwyer](#)

University College Cork

166 PUBLICATIONS 1,516 CITATIONS

[SEE PROFILE](#)

## Metallophosphazene Precursor Routes to the Solid-State Deposition of Metallic and Dielectric Microstructures and Nanostructures on Si and SiO<sub>2</sub>

Carlos Díaz,<sup>\*,†</sup> María Luisa Valenzuela,<sup>‡</sup> Antonio Laguna,<sup>§</sup> Vladimir Lavayen,<sup>||</sup> Josefina Jiménez,<sup>§</sup> Lynn A. Power,<sup>⊥</sup> and Colm O'Dwyer<sup>\*,⊥</sup>

<sup>†</sup>Departamento de Química, Facultad de Ciencias, Universidad de Chile, Las Palmeras 3425, Santiago, Chile,

<sup>‡</sup>Departamento de Ciencias Química, Facultad de Ecología y Recursos Naturales, Universidad Andres Bello, Av. República 275, Santiago, Chile, <sup>§</sup>Departamento de Química Inorgánica, Instituto de Ciencia de Materiales de Aragón, Universidad de Zaragoza-C.S.I.C., 50009 Zaragoza, Spain, <sup>||</sup>Departamento de Física, Universidad Técnica Federico Santa María, Valparaíso 2390123, Chile, and <sup>⊥</sup>Department of Physics and Materials & Surface Science Institute, University of Limerick, Limerick, Ireland

Received January 26, 2010. Revised Manuscript Received March 13, 2010

We present a method for the preparation and deposition of metallic microstructures and nanostructures deposited on silicon and silica surfaces by pyrolysis in air at 800 °C of the corresponding metallophosphazene (cyclic or polymer). Atomic force microscopy studies reveal that the morphology is dependent on the polymeric or oligomeric nature of the phosphazene precursor, on the preparation method used, and on the silicon substrate surface (crystalline or amorphous) and its prior inductively coupled plasma etching treatment. Microscale and nanoscale structures and high-surface-area thin films of gold, palladium, silver, and tin were successfully deposited from their respective newly synthesized precursors. The characteristic morphology of the deposited nanostructures resulted in varied roughness and increased surface area and was observed to be dependent on the precursor and the metal center. In contrast to island formation from noble metal precursors, we also report a coral of SnP<sub>2</sub>O<sub>7</sub> growth on Si and SiO<sub>2</sub> surfaces from the respective Sn polymer precursor, leaving a self-affine fractal structure with a well-defined roughness exponent that appears to be independent (within experimental error) of the average size of the islands. The nature of the precursor will be shown to influence the degree of surface features, and the mechanism of their formation is presented. The method reported here constitutes a new route to the deposition of single-crystal metallic, oxidic, and phosphate nanostructures and thin films on technologically relevant substrates.

### Introduction

Because of their low resistivity and good corrosion resistance, noble metal, transition metal, and silicon thin films have a variety of applications as contacts and conductors in microelectronics and burgeoning nanoelectronics research and eventual development.<sup>1–3</sup> The fabrication of metallic microstructures and nanostructures on dielectric or semiconductor surfaces is a key technology in nanoelectronic engineering. Two principal methods are generally used to prepare metallic thin films—vapor-phase deposition and liquid-based growth—but few thin film methods utilizing precursors in their solid state have been reported.<sup>4</sup> To realize inorganic nanostructured materials,<sup>5</sup> tedious and sometimes expensive methods such as dip-pen nanolithography,<sup>6,7</sup> nanosphere lithography,<sup>8</sup> and ion/electron beam lithography<sup>9</sup>

have been primarily used. For gold and other noble metals, several chemical deposition methods have been reported,<sup>2,9–11</sup> in addition to related electrodeposition techniques.<sup>12</sup> A more sophisticated method using a nanofountain probe to deposit gold particles directly has been recently described,<sup>13</sup> owing to the need for new strategies for particle and structure deposition, including catalyst particles for seeding nanowire growth.<sup>14</sup> The formation of structures with either well-defined or new electrical or optical properties will always be influenced by whether they are formed top down or bottom up. This organometallic and metallic pyrolytic approach to metal structure deposition is inherently bottom up; for certain properties/applications, this is often superior to top-down approaches where feature placement and/or lithography is not a necessity.

In addition to controlled deposition, gold, silver, and other noble metal nanostructures and nanostructured thin films are important in surface-enhanced Raman scattering (SERS), surface-enhanced infrared absorption (SEIRA), localized surface plasmon polariton-based sensors, and surface plasmon-mediated nanostructures for biomolecule detection in the optical near field.<sup>15</sup> Although the

\*Corresponding authors. E-mail: cdiaz@uchile.cl. Tel: +56 2 9787367. E-mail: colm.odwyer@ul.ie. Tel: +353 61 202288.

(1) Forster, S.; Antonietti, M. *Adv. Mater.* **1998**, *7*, 195.

(2) Love, C. J.; Estroff, L. A.; Kriebel, I. J.; Nuzzo, R. G.; Whitesides, G. M. *Chem. Rev.* **2000**, *105*, 1103.

(3) Tao, J.; Cheung, N. W.; Hu, C.; Kang, H. K.; Wong, S. S. *IEEE Electron Device Lett.* **1993**, *13*, 433.

(4) Cao, G. *Nanostructures and Nanomaterials: Synthesis, Properties, & Applications*; Imperial College Press: London, 2004; Chapter 5.

(5) Zhu, F.; Chern, G. W.; Tchernyshov, O.; Zhu, X. C.; Zhu, J. G.; Chien, C. L. *Phys. Rev. Lett.* **2006**, *96*, 027205.

(6) Kuemmel, M.; Allouche, J.; Nicole, L.; Boissiere, C.; Laberty, C.; Ametsch, H.; Sanchez, C.; Gross, D. *Chem. Mater.* **2007**, *19*, 3717.

(7) Hong, S.; Zhu, J.; Mirkin, C. A. *Science* **1999**, *286*, 523.

(8) Zhang, H.; Chung, S. W.; Mirkin, C. A. *Nano Lett.* **2003**, *3*, 43.

(9) Haes, A.; Haynes, C. I.; McFarland, A. D.; Schatz, G. C.; Duyne, R. P. V.; Zou, S. *MRS Bull.* **2005**, *30*, 368. Ding, S.; Qian, W.; Tan, Y.; Wang, Y. *Langmuir* **2006**, *22*, 7105. Gao, H.; Goswami, N. N.; Geng, J.; Tan, L.-S.; Sander, S. *Langmuir* **2006**, *22*, 8078.

(10) Kielbassa, S.; Kinne, M.; Behm, R. J. *Langmuir* **2004**, *20*, 6644.

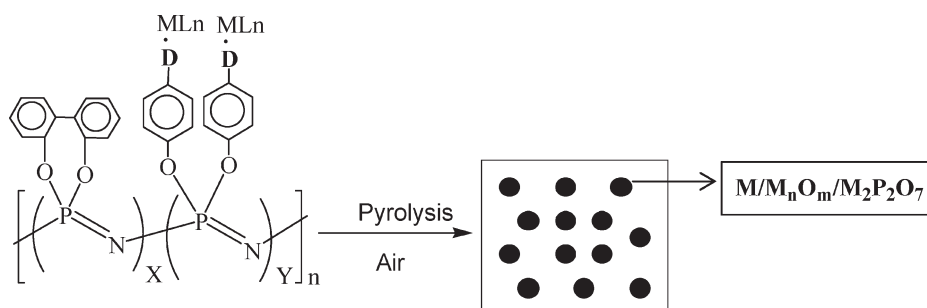
(11) Weiss, E. A.; Kaufman, G. K.; Kriebel, J. K.; Li, Z. H.; Schalek, R.; Whitesides, G. M. *Langmuir* **2007**, *23*, 9686.

(12) Ahn, W.; Taylor, B.; Dall, A. G.; Roper, D. K. *Langmuir* **2008**, *24*, 4174. Michalitsch, R.; Palmer, B. J.; Laibinis, P. E. *Langmuir* **2000**, *16*, 6533. Takami, S.; Jenning, G. K.; Laibinis, P. E. *Langmuir* **2001**, *17*, 441.

(13) Wu, B.; Ho, A.; Moldovan, N.; Espinosa, H. D. *Langmuir* **2007**, *23*, 9120.

(14) Gudiksen, M. S.; Wang, J.; Lieber, C. M. *J. Phys. Chem. B* **2001**, *105*, 4062.

(15) Osawa, M.; Yoshii, K. *Appl. Spectrosc.* **1997**, *51*, 512. Gay, G.; Alloschery, O.; Weiner, J.; Lezec, H. J.; O'Dwyer, C.; Sukharev, M.; Seideman, T. *Nat. Phys.* **2006**, *2*, 792.

**Scheme 1. Schematic Representation of the Preparation Method of Nanoparticles from Polymeric Metallophosphazenes<sup>a</sup>**

<sup>a</sup> Reproduced from ref 18.

fabrication of porous gold, silver, and copper (and many other metals) is relatively straightforward, the realization of SERS/SEIRA deposits on surfaces with other valve and transition metals via designed organometallic routes offers potentially much more flexibility in the phase control of the deposited metals and also in controlled roughness generation and the formation of fractally rough surfaces.<sup>16</sup> This control allows the potential formation of multicatalytic surfaces using Pt- and V-containing organometallic and metallic derivatives of phosphazenes and related macromolecules, for example.

Surprisingly few methods for depositing nanostructured metallic oxides on surfaces via solid-state chemical routes have been reported.<sup>17</sup> Because the formation of individual metal and metal oxide nanostructures and nanostructured films is now possible via this process, metal pyrophosphates are also formed during pyrolysis.<sup>18</sup> This is advantageous because metal pyrophosphates are noted to be good proton conductors in intermediate-temperature fuel cells, and new methods of surface coverage with these compounds are currently being sought.<sup>19</sup> The route that is described here also affords a simple method for positive and negative thermal expansion materials as individual nanostructures or as a deposited film. Pyrophosphates A<sup>IV</sup>M<sub>2</sub>V<sup>V</sup>O<sub>7</sub>, where the A<sup>IV</sup> cation includes Zr, Ti, Mo, Re, W, Th, U, Pu, Ce, Hf, Pb, Sn, Ge, and Si and M<sup>V</sup> = P, V, or As, are known for their unusual high-temperature behavior.<sup>20</sup> Thermal expansion is a necessary consideration in a number of applications where increases and decreases in temperature can affect the physical dimensions, stability, integrity, and mechanical properties of materials; predictably roughened surfaces are also beneficial in maximizing cooling.

Here we present an alternative, simple solid-state process for forming noble metal and pyrophosphate microstructures and nanostructures on Si and SiO<sub>2</sub> surfaces by the pyrolysis of cyclic or polymeric metallophosphazenes requiring neither expensive clean-room nor vacuum equipment to achieve uniphase pure deposition, as summarized in Scheme 1. Considering the interest in the determinate, controlled assembly of nanoparticles and nanostructures on surfaces, the approach reported here allows for a variety of surface coverages with microscale and nanoscale metals, metal oxides, and metal pyrophosphates. We also report

the formation of self-affine fractal transition metal-containing surface films comprising a coral nanostructured SnP<sub>2</sub>O<sub>7</sub> layer.

The phosphazenes used in this work as precursors of microstructures and nanostructures on Si and SiO<sub>2</sub> surfaces are shown in Scheme 2.

## Experimental Section

**Synthesis of Phosphazenes Used as Precursors.** The derivatives containing gold, silver, or tin (**1**, **2**, **4**, **5**, and **6**) were prepared according to published procedures.<sup>21</sup> Polyphosphazene **3** was synthesized using a similar method to that described for **1** and **2** (Supporting Information).

**Preparation and Deposition of the Au, Ag, Pd, and Sn Structures.** *Method A.* A drop of CH<sub>2</sub>Cl<sub>2</sub> solution containing polymer **1** was drained over either a silicon or oxidized silicon surface, and the solvent was evaporated. The concentration of the precursor suspension was always in the range of 10<sup>-3</sup> to 10<sup>-2</sup> g mL<sup>-1</sup>. The Si or SiO<sub>2</sub> wafer (with 400 nm of thermally grown oxide) was subsequently pyrolyzed at 800 °C using a predefined temperature program where the polymer samples were heated at a rate of 10 °C min<sup>-1</sup> from room temperature to 800 °C under a constant air flow of 120 mL min<sup>-1</sup>. The resulting depositions give a uniform areal coverage for each precursor.

*Method B.* The solid polymer was dusted onto the silicon or oxidized silicon wafer polymer/oligomer and pressed with a flat polished metallic surface. The prepyrolytic pressing ensured the best coverage of the solid precursor and minimized locally thicker deposits from the dusting procedure; the sample was then pyrolyzed at 800 °C using the previously described temperature program, also under air.

**Substrate Etching and Cleaning.** The (100) silicon wafer was etched with commercial products SF<sub>6</sub> and C<sub>4</sub>H<sub>8</sub> in an inductively coupled plasma reactor to a typical etch depth of 50–200 nm. It was subsequently cleaned by the standard RCA process and hydrophilized in water.<sup>22</sup>

**Analysis of the Metallic Nanostructured Deposits.** The morphological structure of the metallic structures on silicon and oxidized silicon surfaces using methods A and B was examined by atomic force microscopy (AFM) using a Veeco Enviroscope in contact mode. To analyze the pattern formation, the self-correlated AFM image was processed by the WSxM program. Topological information was supplemented by lateral force and phase modulation imaging to determine adhesion force changes and composition differences in the surfaces examined, respectively. Soft Si<sub>3</sub>N<sub>4</sub>-tipped cantilevers with a spring constant of 0.12 nN nm<sup>-1</sup> were used in contact mode. X-ray diffraction measurements were conducted on a Siemens D-5000 diffractometer with θ–2θ

(16) Berry, M. V.; Hannay, J. H. *Nature* **1978**, *273*, 573.

(17) Barber, Z. H. *Chem. Mater.* **2006**, *16*, 334. Burrel, A. K.; McCleskey, T. M.; Jia, Q. X. *Chem. Commun.* **2008**, 1271. Palgrave, P. G.; Parkin, I. P. *New J. Chem.* **2006**, *30*, 505. Crozier, P. A. *Nano Lett.* **2007**, *8*, 2395. Rao, C. N. R.; Muller, A.; Cheetham, A. K. *The Chemistry of Nanomaterials: Synthesis, Properties and Applications*; Wiley-VCH: Weinheim, Germany, 2004.

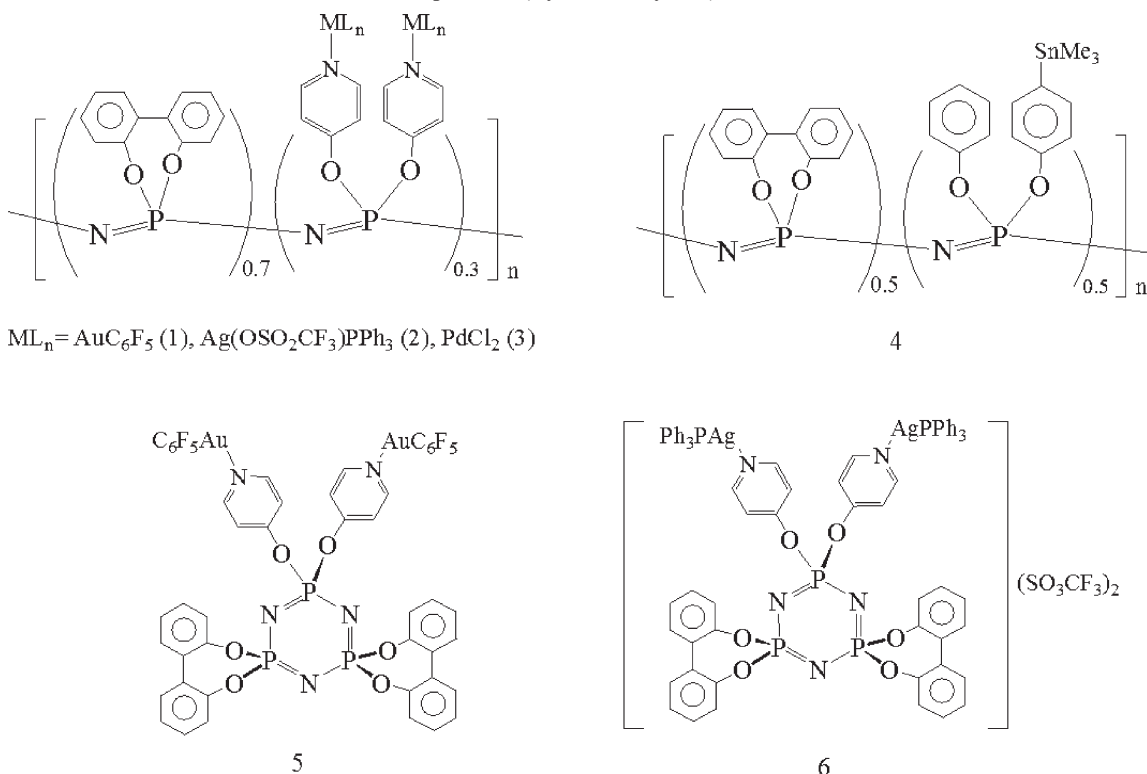
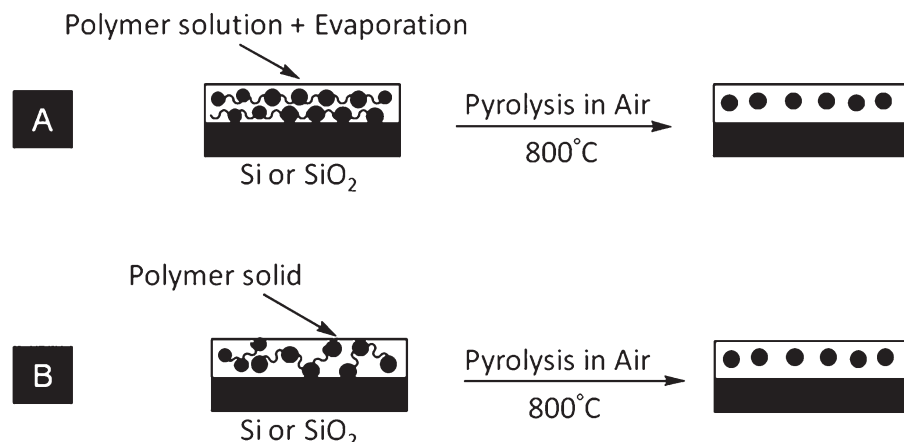
(18) Diaz, C.; Valenzuela, M. L.; Bravo, D.; Lavayen, V.; O'Dwyer, C. *Inorg. Chem.* **2008**, *47*, 11561.

(19) Wu, X.; Verma, A.; Scott, K. *Fuel Cells* **2008**, *8*, 453.

(20) Roy, R.; Agrawal, D. K.; McKinstry, H. A. *Annu. Rev. Mater. Sci.* **1989**, *19*, 59. Sleight, A. W. *Annu. Rev. Mater. Sci.* **1998**, *28*, 29.

(21) Jimenez, J.; Laguna, A.; Benouazzane, M.; Sanz, J. A.; Diaz, C.; Valenzuela, M. L.; Jones, P. G. *Chem.—Eur. J.* **2009**, *15*, 13509. Carriero, G. A.; Valenzuela, M. L.; Diaz, C.; Ushak, S. *Eur. Polym. J.* **2008**, *44*, 686.

(22) Ferrand, P.; Egen, M.; Griseboch, B.; Ahopelto, J.; Mueller, M.; Zentel, R.; Romanov, S. G.; Torres, C. M. S. *Appl. Phys. Lett.* **2002**, *81*, 2689.

**Scheme 2. Formulas of the Phosphazenes (Cyclic or Polymers) Used in This Work as Precursors****Scheme 3. Schematics of the two approaches, Methods A and B,<sup>a</sup> Employed to Create Metallic Nanostructured Surfaces on Si or SiO<sub>2</sub>**

<sup>a</sup> See the main text for a description.

geometry using Cu K $\alpha$  radiation (40 kV, 30 mA). Energy-dispersive X-ray analysis was carried out using a Hitachi SU-70 field-emission scanning electron microscope operating at 10 kV equipped with an Oxford Instruments X-max 50 mm<sup>2</sup> solid-state EDX detector.

## Results and Discussion

**Structure Deposition from the Pyrolysis of the Respective Metallophosphazene.** Methods A and B (Experimental Section) were used to deposit the nanostructured products on Si as well as on SiO<sub>2</sub> surfaces and also on ICP-etched Si surfaces. Scheme 3 shows a schematic illustration of these methods. Because precursors were synthesized for Au, Ag, Pd, and Sn, we first describe the surface morphology and mechanism of deposition of noble metal, metal oxide, and pyrophosphate microstructures and

nanostructures as individual islands and thin films. Figure 1 shows a series of AFM images of the as-deposited structures after pyrolysis of the metallophosphazene derivative directly on the surface using method A. On both Si and SiO<sub>2</sub> surfaces, the product from the Au-containing (Figure 1a,e) precursor (**1**) always forms islands with sizes in the range of 200 nm to 2  $\mu$ m and average heights of 80 nm to 1.6  $\mu$ m. For the more reactive Ag, the pyrolysis of its precursor (**2**) results in quasi-film formation on Si, where the deposit is characterized by a surface coverage interspersed with characteristic craters with an average diameter of 1.3  $\mu$ m. Each of these features is located within a grainlike domain of an Ag deposit. In contrast to Au, the Ag deposit under identical conditions on thermally grown SiO<sub>2</sub> in Figure 1f is markedly different. The surface morphology is characterized a rough deposit of striated Ag structures interspersed by large

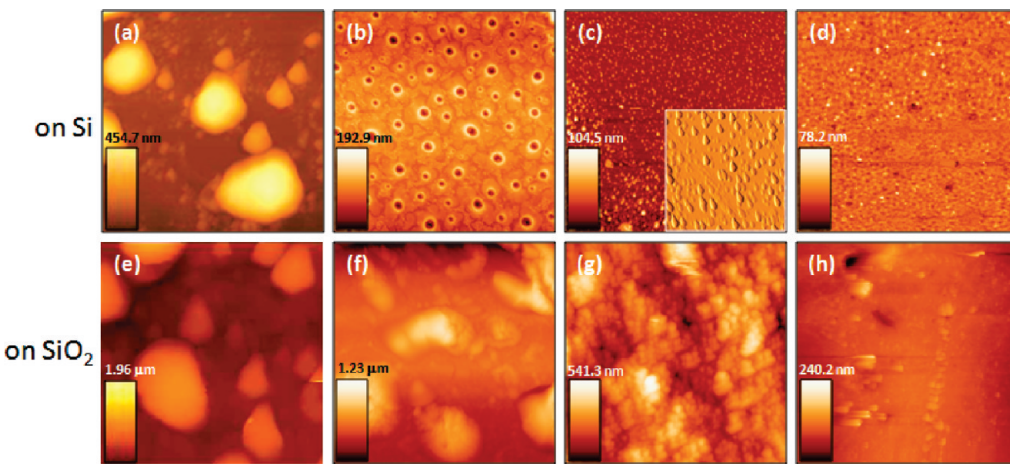


**Figure 1.** Contact mode AFM images of the surface morphology of metallic deposits on (a–d) Si and (e–h)  $\text{SiO}_2$  after the pyrolysis of a series of metallophosphazene precursors using method A: (a, e) Au, (b, f) Ag, (c, g) Pd, and (d, h)  $\text{SnP}_2\text{O}_7$ . See Scheme 2 for details.

hillocks of Ag metal. A shaded AFM image highlighting these features is shown in Supporting Information Figure S1. The feature sizes of Ag on  $\text{SiO}_2$  by this method are similar to that of Au under similar conditions (i.e., islands of  $\sim 1 \mu\text{m}$  height and  $\sim 3 \mu\text{m}$  diameter are found). In general, the tendency of Ag-containing precursors such as **2** is to form films. On Si, the film is incomplete whereas on  $\text{SiO}_2$  the deposition coats the entire surface but also forms locally higher features in the form of hillocks. For the Pd pyrolytic product from **3**, we observe uniformly dispersed and definite tear-drop islands of metal Pd on Si (Figure 1c and inset) and in contrast a very rough thick film deposit of pure Pd on  $\text{SiO}_2$  (Figure 1g). Evidence for the morphology of the individual pear-shaped Pd islands from higher-magnification AFM images is given in Supporting Information Figure S2. As is found by comparing features sizes between Au and Ag deposits (with Ag structures being on average smaller than Au structures), the average feature size of the Pd deposits is  $0.02 \mu\text{m}^2$  (Supporting Information Figure S2), which is smaller than those of Ag and considerably more uniformly dispersed. On Si, this is a useful finding given the catalytic poignancy of a dispersed areal population of pure Pd nanostructures.

For the Sn-containing organometallic derivative of phosphazene, pyrolysis resulted in depositions on Si and  $\text{SiO}_2$  that are markedly different than for noble metals. As shown in Figure 1d,h, the deposition on Si results in a low-roughness film containing a high density of nanoscale structures (outlined in detail further on). On  $\text{SiO}_2$ , however, thick film deposits are routinely observed, where in some instances the uniformity is interrupted by the presence of localized islands. As with all deposits in this work, previous studies<sup>21</sup> have conclusively shown that they are pure metals (except with Ag where some  $\text{Ag}_3(\text{PO}_4)$  phase was also obtained), whereas the Sn-based surface deposit is uniquely pyrophosphate  $\text{SnP}_2\text{O}_7$ .

We conducted careful studies of the true surface roughness of each deposit reported here, and the data is shown in Figure 2, given by

$$R_{\text{rms}} = \left[ \frac{1}{N} \sum_{n=1}^N (y_n^2) \right]^{1/2} \quad (1)$$

where  $N$  is the number of data points of the scan profile and  $y_n$  describe the relative vertical height of the surface. Because the surface comprises several superimposed lateral feature sizes, the measurements are bandwidth limited to a range of  $L/N - L/2$ ,

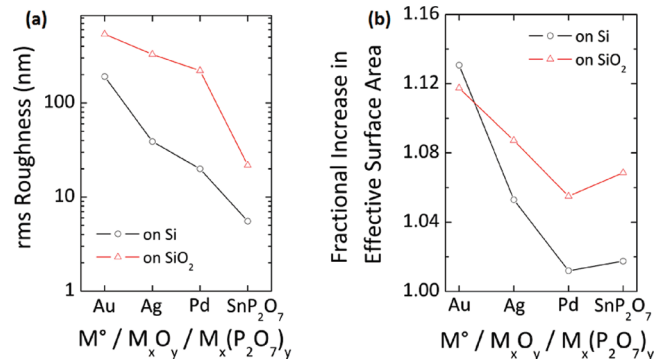


**Figure 2.** (a) Variation in average rms roughness derived from 15 independent scans of surfaces coated with pyrolytic products from Au, Ag, Pd, and  $\text{SnP}_2\text{O}_7$  on Si and  $\text{SiO}_2$ . (b) Fractional increase in surface area as measured from the ratio of the total distance traveled by the tip over the 512 line scans from each image to the distance the tip would travel over the smooth nominal surface area of the Si or  $\text{SiO}_2$  surface.

where  $L$  is the nominal AFM scan length. The typical scan length used here is  $10 \mu\text{m}$ , and the maximum lateral feature length used for the rms calculation is  $\sim 5 \mu\text{m}$ .

The rms roughness, averaged over 15 scans of different regions on each sample, is plotted in Figure 2a, from which we observe a noticeable trend toward lower roughness from the pyrolysis of precursors **1–4**. The highest roughness was observed for Au structures whose deposition is always islands of varied diameter and height, and the lower roughness was observed for  $\text{SnP}_2\text{O}_7$  deposits, which exhibit an rms roughness that is 2 orders of magnitude lower in spite of their rough appearance. The effective increase in surface area was also measured, and the trend, shown in Figure 2b, follows that of the roughness parameter for the noble metals but differs markedly for the pyrophosphate (i.e., the low rms roughness deposits on Si and  $\text{SiO}_2$  of  $\text{SnP}_2\text{O}_7$  exhibit effective surface areas greater than for comparatively rougher noble metal deposits). As will be explained in more detail later, the regularity and small size of the  $\text{SnP}_2\text{O}_7$  structures contribute to this discrepancy where the uniform height of all features contributes to a low rms roughness but AFM tip-radius-corrected surface areas indicate that the real exposed surface area increases by a factor of 1.07. Although an admittedly small change in the effective surface area, it is still greater than the effective surface area of the Pd deposit on Si, which is composed of a high density of nanoscale metallic islands. As with all structures discussed thus

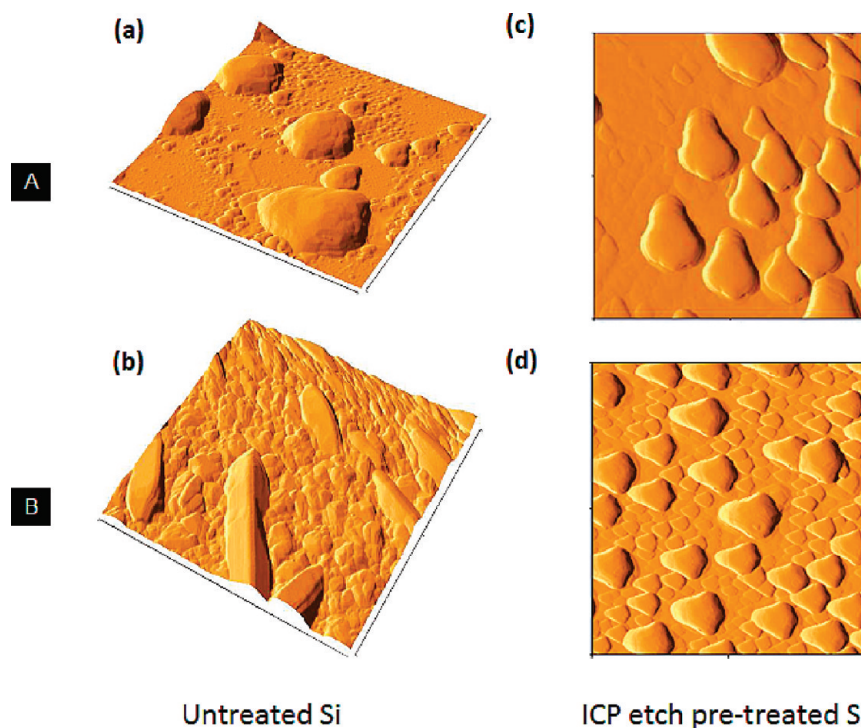


**Figure 3.** AFM images ( $10 \times 10 \mu\text{m}^2$ ) in contact mode for gold deposited on Si by (a) method A and (b) method B. Corresponding scans of the pyrolytic deposition of the Au-containing polymeric precursor (**1**) on Si after inductively coupled plasma etching by (c) liquid state deposition and (d) solid state deposition. Each surface was etched to a depth of 100 nm immediately prior to the placement of either a liquid (method A) or solid (method B) deposit.

far, the predominant trend is for higher roughness and a higher effective surface area on amorphous substrates (thermally grown  $\text{SiO}_2$ ).

The sensitivity of the deposited structures' roughness and surface area to the method of deposition and the substrate was also examined. By using method B for deposition (i.e., by directly placing the solid precursor on Si, followed by pyrolysis, and skipping the solution-based evaporative step), the morphology on Si before and after inductively couple plasma (ICP) etching of the substrate surface was examined. Using the Au-containing polymeric precursor (**1**) as a pertinent example of localized island growth, we find that on untreated monocrystalline Si surfaces islands of various sizes are formed, as shown in Figure 3a (cf. Figure 1a). After the pyrolysis of the solid precursor, however, film deposition is observed to comprise a morphology similar to that of electrodeposited Au (and other metals) with a grainy appearance. Atop such surfaces, we routinely observe Au rodlike features that are several micrometers in length. On the basis of the observations and the mechanism of pyrolysis of organometallic derivatives of phosphazene (discussed further on), the rodlike structures are elongated individual grains. AFM measurements acquired during growth show that these structures form in tandem with the main surface film, although the exact reason for their specific high aspect ratio is as yet unclear.

Deposition on ICP-etched surfaces was also examined. Among the dry etching techniques, ICP is preferable because reactive-ion etching at high-ion energies increases residual lattice damage in the semiconductor and on its surface.<sup>23</sup> However, ICP provides the potential to achieve excellent anisotropy, low surface damage, and smooth surfaces. Figure 3c,d shows the morphology of the Au deposit on ICP-etched Si using methods A and B, respectively.

It is immediately apparent that the shape of the Au islands is more pronounced. In fact, this typical observation of Au on Si has been observed many times and is linked to the relationship with the Si substrate. The Au–Si system has been extensively studied and it therefore appears to be a model system for addressing the growth of metallic nanostructures on a semiconductor surface. Several studies deal with the formation of Au islands on Si.<sup>24</sup> Whereas the majority of these studies focus on the submonolayer coverage of Si with Au and subsequent island growth by the Stranski–Krastanov mechanism<sup>25</sup> occurring at Si(111) step edges, the knowledge is applicable to the present work because the orientation and shape of the islands formed on ICP-etched Si are virtually identical. Increased order in the shape and relative position of the islands was observed after deposition by method B without evaporation, as shown in Figure 3d. The fully formed feature heights do not vary considerably, with typical heights of 320 nm and 365 nm for islands on ICP etched Si deposited by liquid and solid state methods, respectively. No attempt was made here to control or prevent progressive nucleation, and thus the ripeness of the island formation rather than the influence of the substrate and the deposition method on as-pyrolyzed deposits is assessed. It is clear that the highest density of individual Au microstructures is obtained using solid precursors deposited on very smooth ICP-etched Si in spite of the fact that no obvious island formation (as discussed here) is observed by this route on as-received Si surfaces. The fundamental reason for this remarkable difference is related to the surface energy and is currently under study.

**Mechanism of Formation of the Deposited Structures.** The mechanism of formation/deposition of the submicrometer structures on Si and  $\text{SiO}_2$  surfaces by both methods is similar to the formation of other Ru-, W-, Fe-, and Si-containing nanoparticles

(23) Lee, S.-K.; Koo, S.-M.; Zetterling, C.-M.; Östling, M. *J. Electron. Mater.* **2002**, *31*, 340.

(24) Swiech, W.; Bauer, E.; Mundschau, M. *Surf. Sci.* **1991**, *253*, 283.  
(25) Homma, Y.; Finnie, P.; Ogino, T. *Appl. Phys. Lett.* **1999**, *74*, 815.

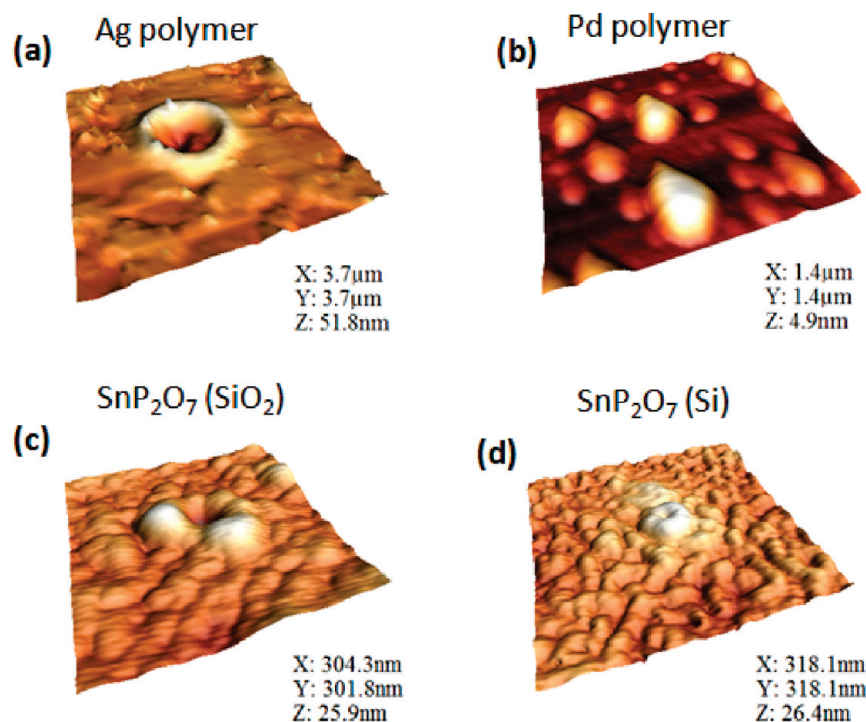


**Figure 4.** AFM images showing the morphology and characteristic features observed in the deposits from pyrolysis on Si of (a) the Ag polymeric precursor (**2**), (b) Pd from polymeric precursor **3**, (c)  $\text{SnP}_2\text{O}_7$  on  $\text{SiO}_2$ , and (d)  $\text{SnP}_2\text{O}_7$  on Si, both from polymeric precursor **4**.

from the pyrolysis of their polyphosphazene precursors.<sup>26</sup> According to this mechanism, the first step involves the oxidation of the carbon atoms of the organic matter arising from bispiro  $\text{O}_2\text{C}_{12}\text{H}_8$  and from the organic groups linked to the metal atoms (i.e.,  $(\text{OC}_5\text{H}_4\text{N})$ ). This step produces a mixture of CO and  $\text{CO}_2$  that form holes in the cyclomatrix, which in turn permits the agglomeration of the metallic centers. This has been verified by TGA/DSC analysis.<sup>18</sup> The CO that is produced reduces the organometallic fragment to the respective metal. The second step corresponds to the oxidation of the phosphorus atoms of the polymeric chain that produces phosphorus oxides as well as to the elimination of fluorine and nitrogen, probably as their respective oxides. As expected, noble metals are not oxidized and remain as  $\text{M}^0$ . Simultaneously, phosphorus atoms arising from the inorganic PN backbone of the polyphosphazenes are also oxidized, forming phosphorus oxides that, by reaction with the metal, form their respective metal pyrophosphates. In this step,  $\text{P}_4\text{O}_7$  is formed and acts as a stabilizer of the metallic nanoparticles, preventing their agglomeration.

From this mechanism, it is expected that the surface morphology and uniformity in deposition would be greatly influenced by the nature of the polymer or trimeric constituent of the precursor. It is now well known that the thermal degradation of cyclotriphosphazenes often produces cyclolinear and cyclomatrix materials<sup>27</sup> influencing the spreading and shape of the pyrolyzed structures.

In Figure 4, we present AFM images of the characteristic features of Ag- and Pd-containing products on Si. In Figure 4a, typical crater formation is observed (cf. Figure 1) and these appear as voids in the pure Ag film. Figure 4b shows the tear-drop

Pd nanostructures. These two depositions are the morphological limits of the precursors investigated: films with voids and the opposite case of individual nanostructures on the bare substrate. For the  $\text{SnP}_2\text{O}_7$  structures (Figure 4c,d) formed by this approach, donut-shaped metal features are observed. These were also observable under SEM (Supporting Information Figure S3). These are similar to the tear-drop Pd structures whose morphology indicates that they are donut-shaped feature without central voids. Thus, once the metal centers agglomerate and pin to the surface, the resulting structural shape or morphology is thus determined by the pyrolytic combustion/decomposition mechanism of the polymer or trimer, as outlined earlier, and the agglomeration of the metal centers.

The influence of the polymeric or cyclic phosphazene precursor on the mechanism of deposit spreading was examined using AFM-based surface morphological measurements of the pyrolytic product from **5** and **6**, which are trimer-based precursors. Figure 5 shows typical AFM images of the Ag and Au surfaces from the pyrolysis of their respective trimeric precursor. The as-deposited Au from trimer precursor **5** shown in Figure 5a exhibits a more irregular deposit with localized Au island formation within a thin film (on both Si and  $\text{SiO}_2$ ). This morphology is in contrast to what is found using polymeric precursors (cf. Figures 1a,e and 4a) where larger islands of greater density are formed. For the Ag deposit, an appreciable difference is observed using derivatives of phosphazenes with a trimeric constituent. Figure 5c,d shows unique morphological features comprising donut-shaped Ag deposits on Si and localized smooth island deposits on  $\text{SiO}_2$ . By comparison with the deposit from the polymeric precursor (cf. Figure 1b,f and Scheme 2), Ag structure deposition on Si from trimeric precursors is characterized by high-density island formation as opposed to cratered thin film formation; evidence of craterlike features is found in some cases (Figure 5c). These structures (from **6**) are directly due to the cross linking of the trimer by metal coordination, producing cyclomatrix structures as shown in Figure 5c.

(26) Díaz, C.; Castillo, P.; Valenzuela, M. L. *J. Clust. Sci.* **2005**, *16*, 51. Díaz, C.; Valenzuela, M. L. *J. Inorg. Organomet. Polym. Mater.* **2006**, *16*, 123. Díaz, C.; Valenzuela, M. L. *Macromolecules* **2006**, *39*, 103. Díaz, C.; Valenzuela, M. L.; Zúñiga, L.; O'Dwyer, C. *J. Inorg. Organomet. Polym. Mater.* **2009**, *19*, 507.

(27) Gleria, M.; Jaeger, R. D. *Applicative Aspects of Cyclotriphosphazenes*; Nova Science Publishers: New York, 2004. Alcock, H. R.; McDonnell, G. S.; Riding, G. H.; Manners, I. *Chem. Mater.* **1990**, *2*, 425. Brown, D. E.; Ramachandra, K.; Carter, K. R.; Allen, C. W. *Macromolecules* **2001**, *34*, 2870.

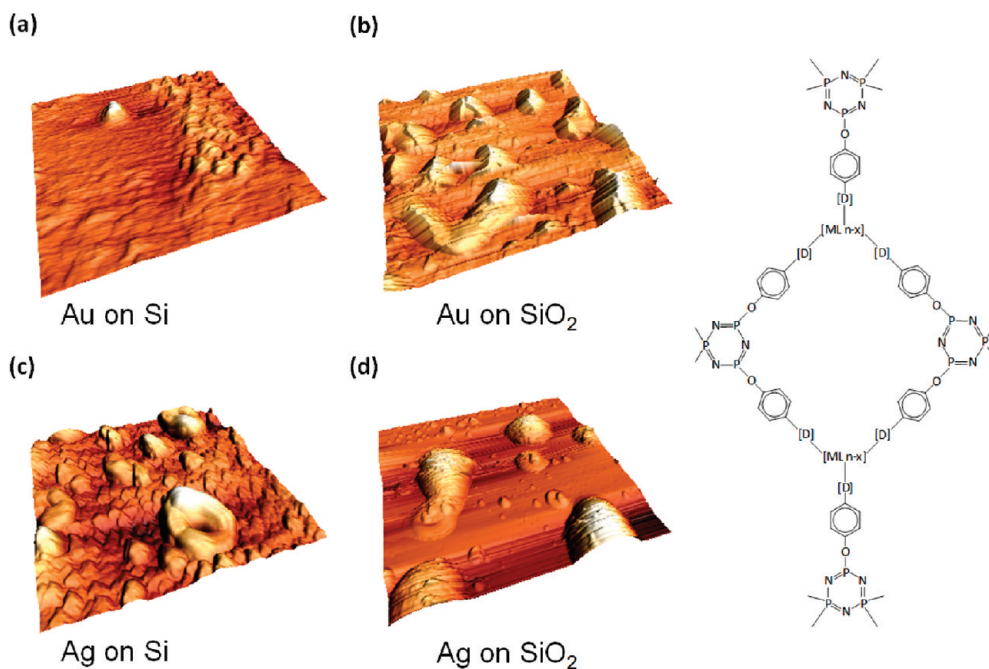


**Figure 5.** AFM images ( $5 \times 5 \mu\text{m}^2$ ) of the deposit morphology from the pyrolysis of trimer-based organometallics containing Au on (a) Si and (b) SiO<sub>2</sub> and also Ag on (c) Si and (d) SiO<sub>2</sub>. (Right) Schematic representation of the cyclomatrix formed during the pyrolysis of metallophosphazene derivatives of a phosphazene trimer.

**High-Areal-Density Pyrophosphate Nanostructure Formation as Self-Affine Fractal Surfaces.** A detailed study of the surface-area coverage of the Sn-based organometallic derivative of phosphazene on Si and SiO<sub>2</sub> was performed to assess the prospect of creating surfaces functionalized with metal networks, which are useful in nanoelectronics and SERS/SEIRA for enhanced adsorbent detection sensitivity as pertinent examples. Normally, noble metal-patterned substrates are studied for SERS and SEIRA effects in addition to catalysis, as principal applications. The goal here is to compare surface deposition characteristics and to draw conclusions regarding the dependence of the surface structure on the preparation procedure. The emphasis is placed on the surface coverage characteristics of the new SnP<sub>2</sub>O<sub>7</sub> deposit. Although the new precursors reported here result in noble metal film and nanostructure deposition on Si and SiO<sub>2</sub>, their complete coverage and grainy films have been studied for decades.

The deposits on Si and SiO<sub>2</sub> are shown in the AFM images of the respective surfaces (Figure 6a–f) using method A. Increasing the resolution of the imaging highlights the high-surface-area labyrinthine nature of the SnP<sub>2</sub>O<sub>7</sub> surface film. XRD studies of the deposit, shown in Figure 6g, indicate single-crystal SnP<sub>2</sub>O<sub>7</sub> formation, and HRSEM investigations summarized in Figure 6h confirm the coral-like nature of the deposit. Details of the morphology were outlined earlier, and higher-magnification AFM images show that this deposit forms as an independent film comprising a nanostructured network of SnP<sub>2</sub>O<sub>7</sub> (Supporting Information Figure S4). Although the long-range similarity in the features is lower for the deposit on SiO<sub>2</sub> possibly because of the amorphous nature of the substrate, the SnP<sub>2</sub>O<sub>7</sub> deposit still forms a quasi-continuous nanostructured film over areas where surface coverage is typically lowest. The detailed fundamental spreading mechanism, to be reported elsewhere, is based on the differences in Hamaker constants<sup>28</sup> for the metals and dielectrics

and their variation as the organic matter carbonizes under thermal excitation on different substrates. This controls the formation of these structures during pyrolysis, but these measurements also show it to be sensitive to the crystallinity of the substrate. The poorest degree of coverage is always found on SiO<sub>2</sub> substrates, which was overcome in our experiments by varying the initial concentration of precursor on that surface.

The influence of temperature during pyrolysis must be considered because it is close to the oxidation temperature of Si (900–1200 °C). The growth rate of thermal SiO<sub>2</sub> is typically diffusion-limited and generally follows the Deal–Grove model, which is suitable for thick oxides on single-crystal silicon.<sup>29</sup> At the pyrolysis temperature of 800 °C, insufficient SiO<sub>2</sub> formation occurs (even when pyrolysis is conducted in air and water vapor initially) to vary the substrate morphology sufficiently and influence or impede the spreading of the organometallic precursor significantly because of continued oxide thickening. In that case, Si atoms would need to diffuse through the thickening oxide and oxygen atoms would need to diffuse through the growing SnP<sub>2</sub>O<sub>7</sub> deposit, both at a temperature lower than that needed for continued diffusion-limited silicon oxidation. Thus, the differences in coverage, which are not completely understood, are related to the carbonization, polymeric dewetting, and metal clustering mechanisms involved during pyrolysis primarily, with little or no oxide thickening (or influence of that thickening).

Figure 7a shows the measured surface profile for SnP<sub>2</sub>O<sub>7</sub> on Si and SiO<sub>2</sub>, averaged over 512 line profiles from several  $0.5 \times 0.5 \mu\text{m}^2$  AFM images in contact mode. It is apparent that the deposits on both Si and SiO<sub>2</sub> are characterized by similar features with average widths of  $\sim 25$  nm. The corresponding average feature area determined from histogram profiles (Figure 7b) of the areal variation in the feature surface coverage is  $\sim 100 \text{ nm}^2$ . Although the average feature sizes are comparable, it is noted that the uppermost surface profile of the deposit on SiO<sub>2</sub> exhibits greater surface relief between structures than that on Si, in

(28) Israelachvili, J. N. *Intermolecular and Surface Forces*; Academic Press: London, 1992.

(29) Deal, B. E.; Grove, A. S. *J. Appl. Phys.* **1965**, *36*, 3770.

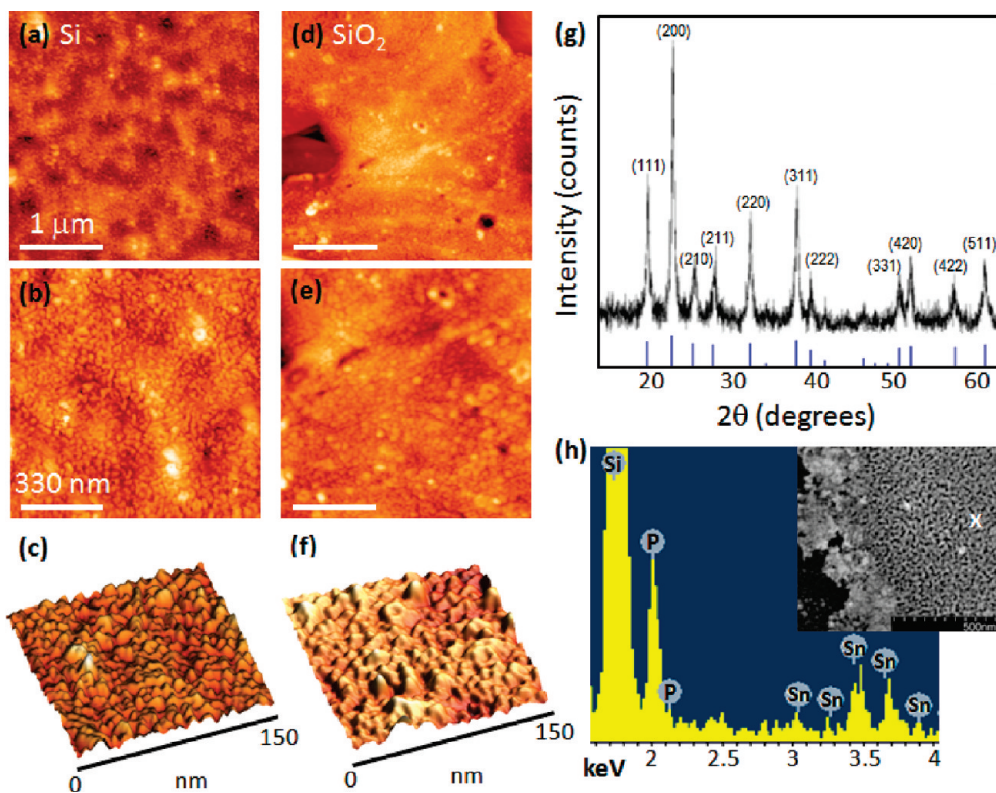


**Figure 6.** Morphological scans of the SnP<sub>2</sub>O<sub>7</sub> product on (a–c) Si and (d–f) SiO<sub>2</sub> at several magnifications. The labyrinthine arrangement of the dielectric SnP<sub>2</sub>O<sub>7</sub> materials is apparent, with greater surface uniformity routinely observed for deposition on Si and a higher density of areal defects (vacancies in coverage) in depositions on SiO<sub>2</sub>. (g) XRD pattern of the pyrolytic SnP<sub>2</sub>O<sub>7</sub> product from **4** displaying only peaks corresponding to tin diphosphate, SnP<sub>2</sub>O<sub>7</sub> (JCPDS card no. 00-029 1352); no peaks for SnO<sub>2</sub> were observed. (h) EDX spectrum acquired from localized regions of the SnP<sub>2</sub>O<sub>7</sub> deposit as shown in the inset; atom % Si K $\alpha$  (85.32); P K $\alpha$  (9.84); and Sn L $\alpha$  (4.84).

agreement with the overall rms roughness of similar deposits summarized in Figure 2 and the morphology in Figure 6c,f. This difference is analogous to the resolution of the feature heights (for a given width) in Figure 7a.

Because AFM scans are a collection of parallel line scans across two dimensions, the resulting line scans that can be analyzed collectively in terms of fractional dimensionality are related to the surface coverage characteristics. Instead of histogram- and counting-based methods, the nanostructured texture of the SnP<sub>2</sub>O<sub>7</sub> deposit over many length scales is analyzed in the framework of a power law dependency where the fitted exponent is related to the surface fractal dimension. The variation of height fluctuations of the structures can be represented through the power spectral density (PSD) where singularities such as peaks can be used to characterize the surface, and thus the deposition, by the use of a spectrum of singularities. This allows us to treat the entire surface deposit as a self-affine fractal structure. The PSD quantity is calculated by performing a Fourier transform of the 2D height data.<sup>30</sup> The Fourier conjugate variable is the spatial frequency that corresponds to the lateral feature sizes, and the strength of the distribution at each spatial frequency corresponds to the average height information for those feature sizes. The PSD is given by<sup>31</sup>

$$\text{PSD}(f) = \frac{1}{f_s L} \left[ \sum_{n=1}^N y_n e^{(-2\pi i f n / N)} \right]^2 \quad (2)$$

Measurements are made over a limited range and with finite resolution, and the PSD is bandwidth-limited with  $L$  being the

total length of the scan and  $f$  being the frequency from  $1/L$  to  $N/2L$ .  $f_s$  is the sampling frequency  $N/L$ . Thus, the PSD provides information across the entire frequency range of the scanned surface from midfrequency jaggedness to lower-frequency form.

The power spectrum for real materials generally obeys a power law and can be characterized by its slope, as is the case for rough surfaces in general.<sup>32</sup> The PSD analysis of the SnP<sub>2</sub>O<sub>7</sub> deposit is given in Figure 7c,d and is described by eq 2. Examples of the areas examined for each substrate in this analysis are shown in Supporting Information Figure S5. The data show linear behavior on a log-log scale, characteristics of a surface exhibiting fractional dimensionality. Repeated measurements on various areas of the surface and corresponding PSD analysis give mean power law exponents of  $-1.78 \pm 0.13$  on Si and  $-1.54 \pm 0.17$  on SiO<sub>2</sub>. These values are clear indications of fractal dimensionality in the morphology of the deposit. Because the rms roughness is the square root of the area under the PSD curve, higher slopes in the power spectrum will result in a lower rms roughness.

In AFM, the analysis of the height–height correlation and the height-difference functions of surface morphologies<sup>33</sup> provides the lateral correlation length of the roughness as well as the roughness exponent  $h$ , which gives information on the localized jaggedness of a surface for a known rms roughness.<sup>34</sup> For such roughness, the height–height correlation function

$$C(x) = \langle [z(x_0 + x) - \langle z \rangle][z(x_0) - \langle z \rangle] \rangle \quad (3)$$

(32) Angelsky, O. V.; Burkovets, D. N.; Kovalchuk, A. V.; Hanson, S. G. *Appl. Opt.* **2002**, *41*, 4620.

(33) Yoshinobu, T.; Iwamoto, A.; Iwasaki, H. *Jpn. J. Appl. Phys.* **1994**, *33*, 383.

(34) Mandelbrot, B. B. *The Fractal Geometry of Nature*; Freeman: New York, 1982. Sinha, S. K.; Sirota, E. B.; Garoff, S.; Stanley, H. B. *Phys. Rev. B* **1988**, *38*, 2297.

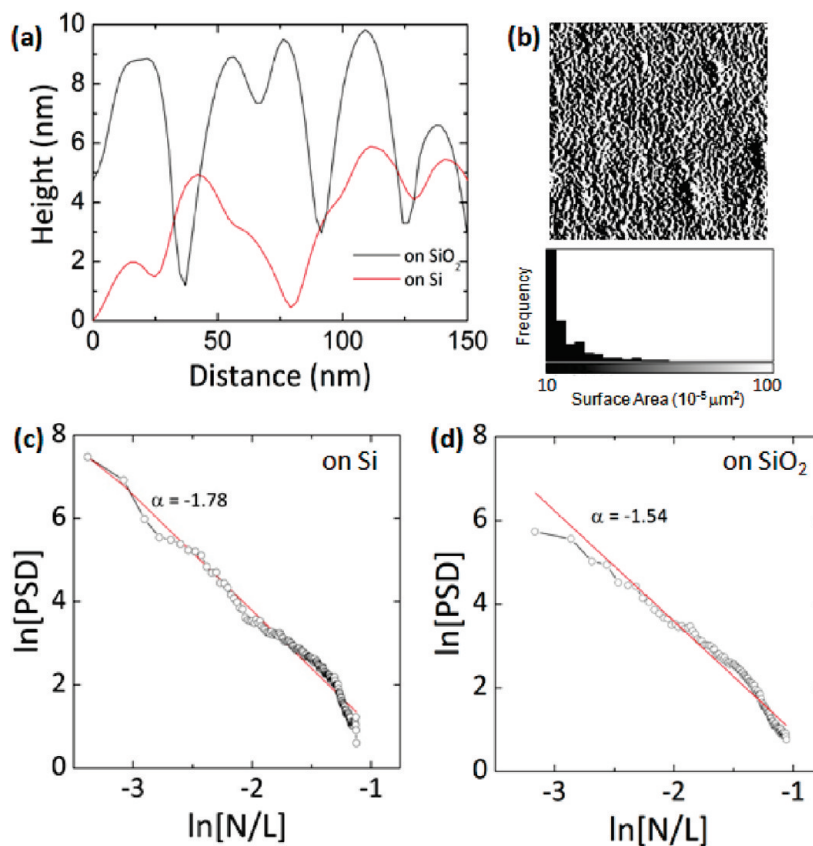


**Figure 7.** (a) Measured surface profile for SnP<sub>2</sub>O<sub>7</sub> on Si and SiO<sub>2</sub>, averaged over 512 line profiles from multiple 0.5 × 0.5 μm<sup>2</sup> AFM scans in contact mode. (b) Histogram of the average surface area of the nanostructured features from the SnP<sub>2</sub>O<sub>7</sub> deposit on Si. Power spectral density analysis of the self-affine fractal surface feature length scale on (c) Si and (d) SiO<sub>2</sub>. Only the Sn-based deposits in this work resulted in fitted exponents in the range of 1.54–1.89 over length scales of 50 nm to 10 μm. The dashed lines indicate the limits of measured slopes for different surface areas in each case.

where  $z(x_0)$  is the height at point  $x_0$  and  $x$  is the lateral separation between two surface points, can be written in terms of  $\sigma$ ,  $\xi$ , and  $h$  as

$$C(x) = \sigma^2 \exp[-(|x|/\xi)^{2h}] \quad (4)$$

where  $\sigma$  is the rms roughness and  $\xi$  is the lateral correlation length given by the value of  $x$  at which the function decays to 1/e. This correlation function also treats the surface as a self-affine fractal<sup>35</sup> on a short length scale and as a smooth surface on a long length scale; the data can then be compared to the roughness and PSD analysis. In this approach, the amount of the diffuse component is determined by the rms roughness. The width of this component and its detailed shape give the lateral correlation length and the roughness parameter, respectively. This approach was successfully applied by Bachelet et al. to show how the intermediate chemically organized surfaces occurring during progressive SrO enrichment of high- $\kappa$  SrTiO<sub>3</sub> can be used as a template for the fabrication of ferromagnetic oxides by chemically driven selective nucleation.<sup>36</sup> In addition, recent studies by AFM of nanostructured carbon films grown by supersonic cluster beam deposition (SCBD)<sup>37</sup> indicate a self-affine fractal structure. This and many other approaches to the fractal description of surfaces are

available, but it is important to point out that most morphological measurements do not give an indication of the scale or correlation of inhomogeneities, which is very beneficial in large-area deposition and self-assembly and aggregation or clustering mechanisms of materials on surfaces. The technique also aids in the roughness analysis of depositions in general by considering all length scales. For the SnP<sub>2</sub>O<sub>7</sub> nanostructured films reported here, we have measured a well-defined roughness exponent of  $h = 0.5 \pm 0.11$  (on Si) and  $0.75 \pm 0.13$  (on SiO<sub>2</sub>) using AFM, which was found to be independent (within the experimental error associated with multiple plots from a range of scan areas on the surface) of the average size of the features. A larger value of roughness parameter  $h$  means more gradual height changes, which verifies the AFM line-scan profiles for the respective surfaces in Figure 7a. In these measurements, the self-affinity has been tested with high-aspect-ratio AFM tips with nominal average radii of 8–10 nm. The roughness exponent of a self-affine film should be independent of the tip radius, provided that the surface correlation and scan lengths are much larger than the tip radius itself. Thus for the present work, no deconvolution of tip radius effects on measured roughness values and surface feature variations is needed.

In addition to studies of the surface fractal dimensions, correlation studies as a function of the length scale were also investigated. Length scales were varied by simply altering the scan lengths for each measurement to probe the self-similarity and long-range order in the deposits expected from power law analysis. Figure 8 shows typical AFM scans of the surface at two length scales together with corresponding self-correlation maps for deposits on Si and SiO<sub>2</sub>. What is observed is that the

(35) Yang, H.-N.; Wang, G.-C.; Lu, T.-M. *Diffraction from Rough Surfaces and Dynamic Growth Fronts*; World Scientific: Singapore, 1993.

(36) Bachelet, R.; Sánchez, F.; Santiso, J.; Munuera, C.; Ocal, C.; Fontcuberta, J. *Chem. Mater.* **2009**, *21*, 2494.

(37) Buzio, R.; Gnecco, E.; Boragno, C.; Valbusa, U.; Piseri, P.; Barborini, E.; Milani, P. *Surf. Sci.* **2000**, *444*, L1.

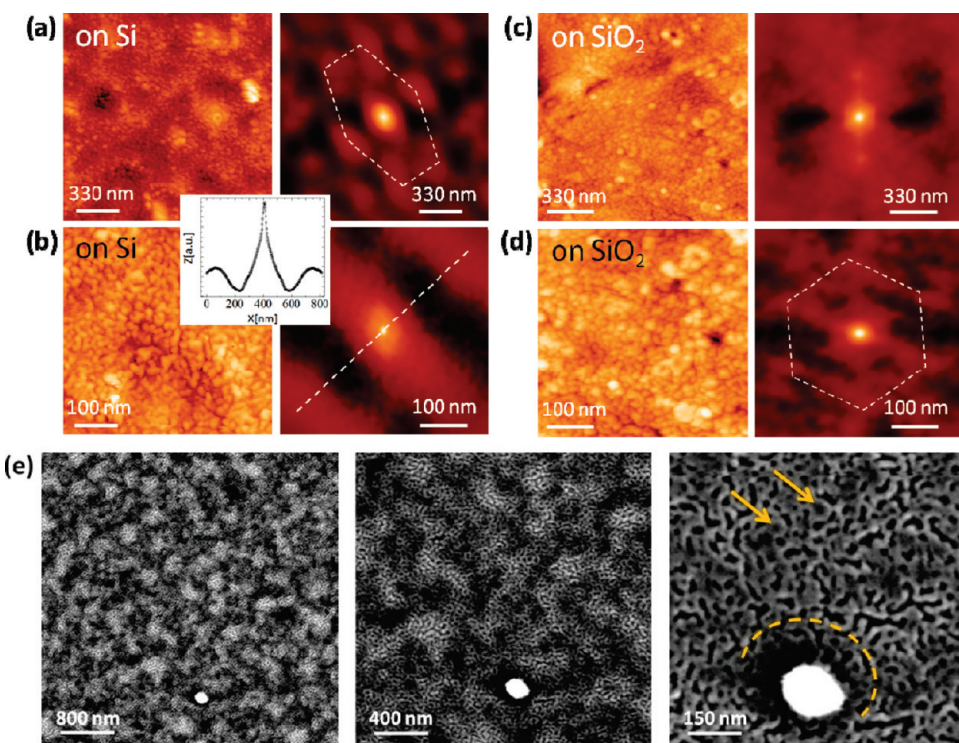


**Figure 8.** (a)  $1.5 \times 1.5 \mu\text{m}^2$  and (b)  $0.5 \times 0.5 \mu\text{m}^2$  AFM images of the SnP<sub>2</sub>O<sub>7</sub> deposit on Si with corresponding correlation length maps. (Inset) Two-dimensional profile corresponding to the dashed line in the correlation map of the AFM image (b, c)  $1.5 \times 1.5 \mu\text{m}^2$  and (d)  $0.5 \times 0.5 \mu\text{m}^2$  AFM images of the SnP<sub>2</sub>O<sub>7</sub> deposit on Si with corresponding correlation length maps. (e) SEM images at successively higher magnifications of a single area of the deposit on Si. The white feature serves as a comparative position marker and also a nucleation point for cyclic SnP<sub>2</sub>O<sub>7</sub>. The dashed arc delineates cyclic structures.

SnP<sub>2</sub>O<sub>7</sub> on Si exhibits two principal spatial correlations: one with a frustrated hexagonal order for longer length scales (Figure 8a) and the second comprising ripples in the self-correlation (Figure 8b). The wavelength of these ripples, shown by the 2D section profile extracted from the self-correlated image in Figure 8b, is  $\lambda = 326 \pm 9 \text{ nm}$ . It must be stated that the scan areas for these measurements were much smaller than for the computed lateral correlation lengths in order to achieve maximal AFM resolution. On slightly longer length scales, we observe both correlations superimposed (Supporting Information Figure S6) where the ripple wavelength is  $\lambda = 296 \pm 17 \text{ nm}$ , similar to what is measured when analyzing short length scales only, as would be expected for a self-affine fractal structure. Direct imaging of the self-affine structure by SEM gives a direct indication of the coral-like deposit. Figure 8e shows the expected self-similar morphology. At lower magnification, the deposit is characterized by varying heights (brighter is higher because of dielectric charging of the surface with impinging electron flux). This is identical to the observations by AFM in Figure 6a. At higher magnification, the features show the finer structure comprising the wavy labyrinthine arrangement of the SnP<sub>2</sub>O<sub>7</sub> clusters, as was observed by AFM. At higher magnification, it is clear that the deposit is dominated by the presence of cyclic structures within the material network. This self-affine spinodal-type organometallic decomposition can be seen specifically in Figure 8e where surrounding the white particle, which acts as a nucleation point during pyrolysis, only cyclic structures are observed. Overall, the deposition is that of a self-affine arrangement of wavy and cyclic SnP<sub>2</sub>O<sub>7</sub> nanostructures in a self-assembled network.

For deposits on SiO<sub>2</sub>, the nanostructured deposit is more irregular (even from the AFM topography images) and does not show any periodic alignment at longer length scales, as judged

by its diffuse self-correlated image in Figure 8c. For short scales, some ordering is apparent and, like the deposit on Si, is represented by a quasi-hexagonal form. The deposit on SiO<sub>2</sub> has less correlated spatial ordering compared to that on Si, but we acknowledge that the more nonuniform deposit over SiO<sub>2</sub> influences the correlation mapping. The stronger self-correlation of the deposit on Si is thus not believed to be linked to the surface crystallinity influence on the deposit morphology per se but is due to the reduced coverage uniformity caused by the noncrystalline, rougher SiO<sub>2</sub> surface.

Thus, from the four individual metals deposited, pyrophosphate exhibits a self-affine fractal surface comprising a labyrinthine arrangement of SnP<sub>2</sub>O<sub>7</sub> on Si and SiO<sub>2</sub> with surface roughness and morphology amenable to several applications requiring high-areal-density nanostructures or deposits. Of course, significant further work beyond the scope of this report is required to state the true fractal nature of the deposit conclusively through multifractal analysis and spectral analysis of the fractal exponents, but it is clear that the deposit exhibits self-affine scaling and is related to the decomposition mechanism of the precursor during pyrolysis.

Because the pyrolysis was conducted in air, the presence of O<sub>2</sub> promotes the spreading of the product.<sup>38</sup> The formation of islands and craters in pyrolyzed precursor-functionalized surfaces is reminiscent of the ramified cluster diffusion mechanism,<sup>39</sup> which can explain the process of spreading on the nanoscale in most studies thus far (i.e., a bulk deposit spread in a ramified manner in the form of agglomerated cluster islands). If this and the

(38) Mestl, G.; Verbruggen, N. F. D.; Lange, F. C.; Tesche, B.; Knözinger, H. *Langmuir* **1996**, *12*, 1817.

(39) Song, Z.; Cai, T.; Chang, Z.; Rodriguez, G. L. A.; Hrbek, J. *J. Am. Chem. Soc.* **2003**, *125*, 8059.

concentration of metal centers play significant roles, as is expected on the basis of the decomposition mechanism outlined earlier, then complete, smooth films could be possible with further study of these precursors as well as the well-defined fractal grain deposition of other metals, oxides, and phosphates on Si and SiO<sub>2</sub>.

## Conclusions

We have demonstrated the fabrication of self-assembled surface deposits of microscale and nanoscale thin films and nanostructured materials of Au, Ag, Pd, and Sn on silicon and silicon dioxide surfaces. The method involves the pyrolysis in air at 800 °C of the respective cyclophosphazene and polyphosphazene containing the metallic derivative. To generate the depositions, liquid-state and solid-state approaches have been used. The morphology of the as-deposited structures depends on the metal used, on the nature of the surface, and on the deposition method.

Noble metals Au and Pd typically form high-areal-density surface deposits of metallic nanostructures, whereas Ag-based precursors form incomplete thin films. The investigation of the precursors by various methods showed the eventual deposition and nanostructure morphology to be influenced by the nature of the polymer or the trimeric constituent of the precursor. In addition, a detailed analysis of the Sn-based deposit showed a well-defined self-affine grainy deposit on Si and SiO<sub>2</sub>, with a characteristics labyrinthine morphology that was shown to have fractional dimensionality and long-range order over many length scales. Method A affords the most uniform coverage for each type of structure, with less control over the resulting morphology coming from method B.

The methods provide the ability to fabricate metallic microstructures and nanostructures and nanostructured thin films on dielectric and semiconductor surfaces, a key technology in nanoelectronic engineering and functionalized surfaces. This solid-state method has potential applications in solid-state devices and for realizing surfaces for SERS, where the fine tuning of the chemistry would allow the rational deposition of controlled shapes and sizes of noble metal microparticles and nanoparticles on technologically relevant substrates with variable smoothness, film thickness, and crystal grain density.

The advantage of this approach over lithographic and physical deposition methods is the site-specific coverage of a surface with nanostructures of a given phase in a simple, cheap manner with clear control over the resulting phase of the deposit. Obviously, for controlled array formation, some lithographic masking must be performed. In comparison to chemical methods, most of which are restricted to Au, the advantage is the versatility. It is sufficient to choose an adequate metallic/organometallic fragment linked to the polymer/oligomer. Pyrolysis will then give the required phase.

The excellent agreement of the AFM-based roughness and PSD analysis data demonstrates the advantage of understanding the deposition of metal oxides and phosphates on Si and SiO<sub>2</sub> by AFM and associated fractal-based analysis. Because depositions of new materials require characterization, metal clusters formed by the approach detailed here are inherently self-assembling and the fractal approach is a useful tool in comparing depositions when the metal center type and concentration are varied to control the morphology for a variety of applications.

**Acknowledgment.** This work was supported by FONDECYT project 1085011. Part of this work was conducted under the framework of the INSPIRE programme, funded by the Irish Government's Programme for Research in Third Level Institutions, Cycle 4, National Development Plan 2007–2013. The Spanish team acknowledges the Spanish Ministerio de Educación y Ciencia (CTQ2007-67273-C02-01) and the Gobierno de Aragón for financial support. We also thank Prof. D. Noel Buckley for access to the Veeco Enviroscope. L.A.P. acknowledges financial support from the University of Limerick.

**Supporting Information Available:** Details of the synthesis of precursor 3, AFM imaging of Pd deposits and their areal density, AFM and SEM imaging of the SnP<sub>2</sub>O<sub>7</sub> surface features, and long-range AFM-based self-correlation analysis of the Sn-based deposit. This material is available free of charge via the Internet at <http://pubs.acs.org>.